

Estimation of topographical effects at Narni ridge (Central Italy): comparisons between experimental results and numerical modelling

Lovati S., Bakavoli M.K.H., Massa M., Ferretti G., Pacor F., Paolucci R., Haghshenas E. and Kamalian M.

Corresponding author: sara.lovati@mi.ingv.it

Abstract

In the present work the seismic site response of Narni ridge (central Italy) is evaluated by comparing experimental results and numerical simulations. The inhabited village of Narni is located in central Apennines at the top of a steep massive limestone ridge. From March to September 2009 the site was instrumented with 10 weak-motion stations, 3 of which located at the base of the ridge and 7 at the top. The velocimetric network recorded 642 events of M_L up to 5.3 and hypocentral distance up to about 100 km. The great amount of data are related to the April 2009 L'Aquila sequence. The site response was analyzed using both reference (SSR, Standard Spectral Ratio) and non reference spectral techniques (HVSr, Horizontal to Vertical Spectral Ratio). Moreover directional analyses were performed in order to evaluate the influence of the ridge orientation with respect to the selected source-site paths. In general the experimental results show amplification factors for frequencies between 4 and 5 Hz for almost all stations installed along the crest. The SSR technique provides amplification factors up to 4.5 in a direction perpendicular to the main elongation of the ridge. The results obtained from the data analyses were used as a target for bidimensional and tridimensional numerical simulations, performed using a hybrid finite-boundary element method and a boundary element method for 2D and 3D modelling respectively. In general, the results obtained through numerical simulation fit well the experimental data in terms of range of amplified frequencies, but they underestimate by a factor of about 2 the observed amplifications.

Key words: topographical effects, spectral analyses, directional analyses, vertical amplification, numerical modelling

Introduction

Macroseismic observations of damage after destructive earthquakes on irregular topography suggest that a morphological irregularity plays a significant role in the propagation of seismic waves. The focusing of seismic waves near the crest of a hill due to the reflection on free surface and the interaction between incident and diffracted waves (Bard, 1982) or the resonance of the whole relief when the wavelength of the incident seismic-field is comparable with the horizontal width of the mountain (Faccioli et al., 2002) are examples of physical phenomena that cause the spatial variability of seismic waves on an isolated relief. In the last years, amplifications at the top of mountains were discussed and well documented both through experimental studies (i.e. Spudich

et al., 1996; Le Brun et al., 1999; Massa et al., 2004 and 2010; Buech et al., 2010; Pischiutta et al., 2010; Marzorati et al., 2011) and 2D and/or 3D numerical modeling (i.e. Boore, 1972; Bard and Tucker, 1985; Geli et al., 1988; Sanchez-Sesma, 1990; Sanchez-Sesma and Campillo, 1991; Chavez-Garcia et al., 1996; Komatitsch and Vilotte, 1998; Paolucci, 1999; Paolucci, 2002, Kamalian et al., 2006 and 2007).

In this case, different approaches used to investigate the same issue allow to evaluate possible discrepancies between the results obtained by numerical simulations with respect to those obtained by experimental methods. Concerning the latter ones, the main causes of uncertainties concerning the interpretation of the results are represented by the difficulty both to select a relief characterized by a massive geological formation without relevant anisotropy (able to modify the wave-field during its propagation path) and by the possibility to install at the base a reference station located on the same geological formation that characterizes the whole morphological body. Only in this way it is possible to evaluate the actual effect due to the topography and isolate it from other causes of amplification such as stratigraphic or near fault effects (Le Brun et al., 1999; Paolucci et al., 1999; Rovelli et al., 2002).

Concerning the numerical modelling, besides the difficulty to solve in many cases complex geometric configurations, the main problem is often represented by the lack of geological and geotechnical information related to the investigated site. The methods more widely used are the finite difference method (Boore, 1972; Zahradnik and Urban, 1984), the finite element method (Smith, 1975), the integral equation method (Sills, 1978), the boundary element methods (Sanchez-Sesma et al., 1982), the discrete wave-number methods (Bouchon, 1973; Bard, 1982) and the spectral element methods (Faccioli et al., 1997; Komatitsch D. and Vilotte J.P., 1998). In general the common result of modelling, if compared with experimental methods, is the underestimation of the amplification factors if compared to those obtained by experimental data. The main cause is generally attributed to simplified 2D or 3D geometries of topographic reliefs (coupled to non homogeneous soil conditions and simplified plane wave input assumptions) that are not able to well reproduce the complexity of real cases.

In the framework of the 2007-2009 agreement between INGV (Istituto Nazionale di Geofisica e Vulcanologia) and DPC (Italian Civil Protection), the S4-Project founded the installation of 7 velocimetric station from March to September 2009 in correspondence of Narni ridge (Central Italy) with the aim to detect possible seismic amplifications due to the topography. Since 1974, in correspondence of this site, a strong-motion station (named NRN, see <http://itaca.mi.ingv.it>) belonging to the Italian Accelerometric Network (RAN) is installed.

As a matter of fact, topographic irregularities are a common feature of many sites of installation of strong motion stations included in the ITACA database (Pacor et al., 2010, this issue), thus deserving a specific care for their seismic characterization. Preliminary analyses on the experimental data are described in Massa et al. (2010). This paper is especially focused on the

comparison between the experimental results, obtained applying both the single station technique (Horizontal to Vertical Spectral Ratio, HVSR, Lermo and Chavez-Garcia, 1993) and the reference station technique (Standard Spectral Ratio, SSR, Borchardt, 1970) and those coming from numerical modelling. The simulations were performed both in 2D configurations, using the code based on hybrid finite-boundary element method (Kamalian et al., 2003) and in 3D configurations, using the BEMSA code (Sohrabi et al., 2009) based on the boundary element method.

The Narni field experiment

Narni is a little village built at the top of a morphological ridge in central Apennines (inset in the bottom panel of figure 1). The studied ridge, oriented N31°W and approximately 1.3 km long, is characterized by a difference of quota between the top and the base ranging from 100 m in correspondence of the NW edge (close to NRN9 station) to 220 m in correspondence of the NRN4 station (Figure 1, bottom panel). The width of the ridge ranges from about 400 m, in the Northwestern part, to about 800 m in the Southeastern one (Figure 1, bottom panel). The transverse section of the hill is characterized by an evident asymmetry, being the Western and the Eastern slope as steep as 35° and 22°, respectively. From a geological point of view, the site is characterized by a massive limestone formation (Figure 1, bottom panel), with a negligible level of fracturation (Geological Map of Italy, 1:100.000, sheet 138; Amanti et al., 2002).

On the basis of the new Italian technical rules for design of buildings (Norme Tecniche per le Costruzioni, NTC, 2008) Narni ridge might be included in a category that falls between T3 (on the basis of Eastern slope) and T4 (on the basis of Western slope). In general, according to NTC 2008, Italian topographies are classified in four categories (from T1 to T4 depending on the geometry of the relief). Topographic amplification is taken into account through a correction coefficient factor (S_T from 1.0 to 1.4, period independent) to be applied to the horizontal acceleration response spectra defined for a rock site. The definition of S_T is essentially based on 2D numerical analyses and therefore it is properly applicable only to crests of elongated ridges (difference between top and bottom higher than 30 m).

With the aim to evaluate possible seismic ground motion amplification due to the morphological setting of the investigated site, from March 2009 to September 2009 a temporary velocimetric network was installed in Narni and surroundings. During this period 7 seismic stations were employed in order to monitor a total of 10 different sites. The stations NRN2, NRN3 and NRN5 were installed at the base of the ridge, the stations NRN9, NR10, NRN6, NRN7, NRN8 and NRN4 (from Northwest to Southeast) were installed along the top of the ridge and the NRN1 station were installed along the flank of the Eastern slope (Figure 1, bottom panel). All stations were equipped with Lennartz LE3D-5s sensors coupled with 24 bits data loggers (Reftek 130/01 and Lennartz MarsLite). During the period of installation a dataset of 642 earthquakes, characterized by local magnitude (M_L) between 1.5 and 5.3 and maximum epicentral distance from Narni of about 100

Km, was collected. It is worth noting that the great amount of data (about 90%) are related to the April 2009 L'Aquila sequence (Ameri et al., 2009). The left panel of Figure 2 shows the location of all recorded events while in the right panel the distribution of magnitude versus hypocentral distance, divided according to the azimuth direction, is reported. In both panels of Figure 2, the dashed inset indicates the earthquakes with M_L from 1.5 to 3.6 occurred at an epicentral distance smaller than 50 km from Narni.

Experimental results

The data collected during the field experiment were analyzed in single station (HVSR) and reference site (SSR) approach. In the last case NRN2 station (Figure 1, bottom panel), installed on limestone outcropping at the base of the ridge, was selected as a reference. During the analyses different sub sets of events were selected in order to consider different portion of signal (S-phase and coda) and different ranges of epicentral distance and source to site azimuths. In all cases, directional analyses (rotation of north-south component clockwise from 0° to 175° , with angular step of 5°) were computed in order to investigate if the ground motion recorded at stations installed along the crest undergone polarization effects. The signals were processed by removing the mean and the linear trend and by applying an acausal 4-pole Butterworth band-pass filter in the range 0.2 - 25 Hz. Before calculating the spectral ratios, all Fourier spectra were smoothed by applying a Konno-Omachi window ($b=20$). It is worth noting that in this paper only the meaningful experimental results, in particular those concerning NRN7 and NRN4 (the two stations located in correspondence of the two modelled profiles P1 and P2, see bottom panel of figure 1) are presented. A more comprehensive description of experimental analyses, concerning all stations, can be found in Massa et al. (2010).

In figure 3 the directional HVSRs obtained considering 27 events (M_L from 1.5 to 3.6) with epicentral distance up to 30 Km from Narni (Figure 2) are shown. In the top panels of figure 3 the results for the reference station (NRN2), located at the base of the ridge, and for NRN1, installed in the middle of the Eastern slope (average slope of about 22°), are presented: for both stations no clear amplification peaks were detected. In the bottom panels of the same figure the results for two stations installed at the top of the ridge are shown: NRN7, located at the break of the west-side slope (average slope of about 35°) and NRN4, located at the highest point of Narni ridge. In this case the directional HVSRs show amplification around 4 Hz for NRN7 and between 4 and 6 Hz for NRN4. For both stations, clear polarization effects are present for directions between 60° and 100° (see legend in the figure). Considering that the ridge is oriented N- 30° W this means that the highest amplifications were detected for directions perpendicular to the main elongation of the hill: this evidence was already pointed out in recent papers concerning on the experimental seismic response of topographic irregularities (e.g. Spudich et al., 1996; Le Brun et al., 1999; Buech et al., 2010; Massa et al., 2010; Pischiutta et al., 2010; Marzorati et al. 2011).

Concerning the directional SSRs, the results are presented for NRN7 (left panels) and for NRN4 (right panels) stations in figure 4. In the left panels the influence of the analysed portion of signal is highlighted. For NRN7 the same events selected for HVSRs (M_L from 1.5 to 3.6 and epicentral distance up to 30 Km) were considered. In the top-left the results obtained by analysing 10 s of S-phase are shown: in this case two amplification peaks are evident, the first around 2 Hz and the second in the range 4-5 Hz, both clearly polarized in the direction 60° - 100° . The SSRs presented in the bottom-left, obtained considering 10 s of coda, show again the amplification peak around 4.5 Hz due to the topography. On the contrary the amplification peak at 2 Hz disappears, pointing out a different origin of this peak, probably due to source effects of small events occurred very close to the ridge (the great amount of selected events have distances lower than 15 km).

Right panels of figure 4 show comparisons between SSRs calculated for NRN4 station, considering at first all 27 events (top-right panel) and then a sub set of 14 events with source to site azimuths with directions perpendicular to the main elongation of the ridge (bottom-right panel). Even if in both cases the results show amplification peaks between 3.5 and 5.5 Hz (polarized in the direction 60° - 100°), in the bottom panel higher amplifications are observed.

In figure 5 some results of vertical SSRs computed considering both weak motion (black lines), recorded in near field and strong motion (April 2009 L'Aquila sequence) recorded in far field (red lines) are presented. Even for vertical component non negligible amplifications are present for the stations installed at the top of the hill: with the exception of NRN1, where no amplification peaks are detected, the other analysed stations (NRN7 in the left top panel, NRN4 in the right top panel and NR10 in the left bottom panel) show amplification factors between 3 and 4 involving frequencies between 3 and 6 Hz. Only for NRN4 amplifications also at higher frequencies (up to 10 Hz) are present.

Numerical modelling: theoretical background

The numerical simulations were executed using the well known time domain Boundary Element Method (BEM), based on 2D and 3D elastodynamic equations. The governing relation for an elastic, isotropic and homogeneous body, with a small amplitude displacement field, is

$$(c_1^2 - c_2^2) \cdot u_{j,ij}(x,t) + c_2^2 \cdot u_{i,ij}(x,t) + b_i(x,t) - \ddot{u}(x,t)_i = 0 \quad (1)$$

where c_1 and c_2 are the propagation velocities for the longitudinal and transverse waves respectively, u denote the displacement vector and b_i denotes the body force vector. The term c_1 is given by

$$c_1^2 = (\lambda + 2\mu) / \rho \quad (2)$$

while the term c_2 is given by

$$c_2^2 = \mu / \rho \quad (3)$$

In equations (2) and (3) λ and μ are the Lamé constants and ρ is the density. The corresponding governing boundary integral equation for an elastic, isotropic and homogeneous body can be obtained using the well known weighted residual method (Brebbia and Dominguez, 1989), written in the form

$$c_{ij}(\xi) \cdot u_i(\xi, t) = \int_{\Gamma} (G_{ij} * t_i(x, t) - F_{ij} * u_i(x, t)) d\Gamma \quad (4)$$

where c_{ij} denotes the discontinuity term resulting from the singularity of the F_{ij} fundamental solutions, u_i is the displacement vector, G_{ij} and F_{ij} are the transient displacement and traction fundamental solutions respectively. They represent displacements and tractions at a point x and at time t due to a unit point force applied at point ξ at previous time $t = \tau$. The terms $G_{ij} * t_i$ and $F_{ij} * u_i$ are the Riemann convolution integrals and t_i represents the traction at the boundary. In the equation 4, the contributions due to the initial conditions and to the body forces are neglected. The implementation of the boundary integral equation needs approximation in both temporal and spatial variations of field variables. A detailed introduction of BEM, implemented in the numerical codes used in this study, can be found in Kamalian et al. (2003).

In the case of a topographic irregularity, the frequency response at the surface of a 3D body can be expressed in the form

$$\begin{Bmatrix} O_1^k(f) \\ O_2^k(f) \\ O_3^k(f) \end{Bmatrix} = \begin{bmatrix} H_{11}^k(f) & H_{12}^k(f) & H_{13}^k(f) \\ H_{21}^k(f) & H_{22}^k(f) & H_{23}^k(f) \\ H_{31}^k(f) & H_{32}^k(f) & H_{33}^k(f) \end{bmatrix} \cdot \begin{Bmatrix} I_1(f) \\ I_2(f) \\ I_3(f) \end{Bmatrix} \quad (5)$$

In equation (5), the term O_i^k denotes the i_{th} component of ground motion at a generic point k located on the free surface of the topography, I_i is the corresponding ground motion at the base of the topography (reference site) and H_{ij}^k is the transfer function for a point k in the i_{th} direction due to an incident harmonic motion, with unit amplitude, oriented along j_{th} direction (Paolucci, 1999). The non diagonal elements in the H matrix of equation 5 represent the cross-coupling term

(Paolucci 1999). For 2D simulations the equation is simplified, because it does not consider the terms referring to the third direction (e.g. $O_3^k(f)$ etc.).

In order to calculate the transfer functions, three independent 3D (or two independent 2D) numerical simulations were performed in time domain. For each analysis, the input consisted of a vertically incident Ricker wavelets (along each spatial direction) expressed as defined in the equation 6:

$$f(t) = A_{\max} \cdot \left[1 - 2 \cdot (\pi \cdot f_p \cdot (t - t_0))^2 \right] \exp^{-(\pi \cdot f_p \cdot (t - t_0))^2} \quad (6)$$

The terms A_{\max} , f_p and t_0 denote the maximum amplitude of the time history, the predominant frequency and the time shift. For instance, once the model is excited by vertically propagating S-waves (X-polarization and Y-polarization) independently, the H_{11} , H_{21} , H_{31} and H_{12} , H_{22} , H_{32} can be evaluated, respectively. Then the model will be impinged by vertically incidence of P-waves in order to extract H_{13} , H_{23} and H_{33} .

For deriving 2D transfer function components, the aforementioned time domain analysis will be limited to simply two independent P-SV analyses. For example, in order to determine $H_{21}^k(f)$, a time domain analysis was performed using the input motion oriented along x-axis, e.g. SV wave, then the Fourier transform of the response at k^{th} receiver point along y-axis ($O_2^k(f)$) would be determined, and the spectral ratio $H_{21}^k(f) = O_2^k(f) / I_1(f)$ would be easily calculated.

For each receiver point along a generic topographic profile, H_{ij}^k synthetic functions are available and consequently it is possible to compare for each station experimental and synthetic results.

2D site response : results

The 2D simulations were performed by using the *HYBRID* code, developed by Kamalian et al. (2003) and already tested for several examples of site response concerning canyons and hills (Kamalian et al. 2006; 2007). To further verify the capability of *HYBRID*, we investigated the response of Narni ridge in correspondence of two transversal profiles (P1 and P2, see figure 1) that crossed the two stations (NRN7 and NRN4 respectively), showing the highest experimental amplification values.

The models of the two transverse profile, 1050 m long for P1 and 1670 m long for P2, were discretized using 499 nodes spaced in average 14 m for P1 and 20 m for P2 (in the neighbourhood of the topography).

The criterion used for discretization in boundary element is based on Israil and Banerjee's approach (1990). The time step should be chosen in a way that the wave travels between 50 % to 75 % of the element length at that time, following the relation (7)

$$^a t \times V \sim 0.5 \sim 0.75 L \quad (7)$$

where $^a t$ is time step, V is the propagation velocity and L is the length of the element. Being the half length of the element supposed to be 14 m and 20 m for the two profiles, considering $V_s = 1000$ m/s and $^a t = 0.025$ s the above inequality was satisfied.

In both cases the models were characterized by 249 quadratic boundary elements. The half space, around the profiles, crossing Narni ridge, was discretized up to eight times the profiles length with a gradual increase in element dimensions.

The profiles were modelled considering a shear wave velocity of 1000 m/s, a Poisson's ratio of 0.37 and a density of 2.3 t/m^3 . The information about the material properties comes from a down-hole test (Regione Umbria, 2001) performed in correspondence of a massive limestone formation outcropping about 5 km South-West of Narni.

In the current work, A_{\max} , f_p and t_0 of equation (6) were set to 0.001 m, 3 Hz, and 0.7 s, respectively. In this way it is possible to investigate the frequency range 1-8 Hz.

In general, once theoretical transfer functions H_{ij} are available, SSRs and HVSRs for receivers located along the profiles can be easily derived using equations (8) and (9), where I_i^k is the spectrum calculated considering a real seismogram recorded at the reference site and O_i^k is the spectrum obtained at the top of the topography multiplying the reference site spectrum by the theoretical transfer function H_{ij}

$$SSR_1^k(f) = \left| O_1^k(f) / I_1^k(f) \right| = \left| \frac{[H_{11}^k(f) \cdot I_1(f) + H_{12}^k(f) \cdot I_2(f) + H_{13}^k(f) \cdot I_3(f)]}{I_1^k(f)} \right| \quad (8)$$

$$HV_1^k(f) = \left| O_1^k(f) / O_3^k(f) \right| = \left| \frac{[H_{11}^k(f) \cdot I_1(f) + H_{12}^k(f) \cdot I_2(f) + H_{13}^k(f) \cdot I_3(f)]}{[H_{31}^k(f) \cdot I_1(f) + H_{32}^k(f) \cdot I_2(f) + H_{33}^k(f) \cdot I_3(f)]} \right| \quad (9)$$

As noted before, for 2D simulations equations 8 and 9 can be rewritten by ignoring the terms related to the third direction (e.g. H_{13} , H_{31} etc).

It is worth noting that in our case the cross-coupling terms (also for 3D case) were found very close to zero. Therefore, following equation (8), the SSRs computation does not depend on the input motion and, as a consequence, the value of the ratio closely approaches to the transfer function H_{ij} , as demonstrated in the equation (10)

$$SSR_1^k(f) = \left| [H_{11}^k(f) \cdot I_1(f)] / I_1^k(f) \right| = H_{11}^k(f) \quad (10)$$

As shown in figures 7, 9, 11 and 12 (left panels) the SSRs are characterized by very small scatter, only dependent on the negligible contribution of the cross-coupling terms. Moreover, since the considered code does not take into account both magnitude (source) and distance (attenuation) contributions and being the cross-coupling terms (e.g. $H_{12}^k(f)$, $H_{13}^k(f)$) close to zero, whatever seismogram is used the SSR results do not depend on the input motion. In this way the SSRs shown in figures 7, 9, 11 and 12 (left panels) describe the behaviour of an half-space vertically excited by an incident plane wave.

On the contrary, following the formula (9) the computation of HVSR is simplified as (11)

$$HV_1^k(f) = \frac{H_{11}^k(f) \cdot I_1(f)}{H_{33}^k(f) \cdot I_3(f)} = \frac{H_{11}^k(f)}{H_{33}^k(f)} \cdot \frac{I_1(f)}{I_3(f)} = Const \cdot \frac{I_1(f)}{I_3(f)} \quad (11)$$

In this case, being the ratio dependent to the input motions, the variation in the results is not negligible (see right panels in figure 7, 9, 11 and 12).

Seismic response of profile 1

Figure 6 (top panel) shows the general pattern of amplification ratio (in term of transfer functions H_{11}) estimated for all receivers located along P1 (crossing the NRN7 station, middle panel of figure 6) excited by vertically propagating SV-Ricker wavelets.

From the top panel of figure 6 it can be deduced that the fundamental vibration mode of the hill, involving in-phase motion of the whole topography is around 1 Hz. Following the analytical simple formula proposed by Geli et al., 1988 (12),

$$f_0 = V_s/L \times (0.4) \quad (12)$$

where f_0 is the resonance frequency, V_s is the shear wave velocity and L is the semi-width of the mountain, considering for Narni a transverse width ranging from 500 m to 800 m (see figure 1, bottom panel) and a V_s of 1000 m/s (on the basis of the down-hole performed on the same formation during the 2001 Regione Umbria microzonation studies), the obtained theoretical resonance frequency ranges from 1.0 to 1.6 Hz. It is worth noting that the only experimental evidence of amplification peak around 1 Hz was found analyzing the 16th December 2000, M_L 4.1, earthquake, occurred at a epicentral distance of 5 km East of Narni ridge (Massa et al. 2010).

However, as shown in the same figure, the peak of the amplification function is for a higher mode, around 4-5 Hz. The maximum amplification at such frequency is at the crest and rapidly decays towards the bases, involving de-amplification effects at mid-height of the hill. Figure 6 (bottom panel) depicts the time domain response for horizontal component for the profile P1 subjected to a vertically propagating incident SV wave. The pattern of diffraction and refraction can be clearly

seen. The maximum amplitude occurred at the top of the hill due to focusing of energy and interference between the incident and diffracted waves.

As explained before, P-SV analyses were carried out for deriving transfer functions useful to study the hill response under multi-component excitation. By calculating different components of transfer function matrix for the receiver points and carrying out convolution analysis, spectral ratios were extracted using equations 8 and 9. In these equations I_1 , I_2 and I_3 (i.e. I_1 and I_2 for 2D simulation) represent the seismograms recorded by the station used as a reference in the experimental analyses (NRN2). Both SSR and HVSR were calculated considering 27 weak motions with $1.5 \leq M_L \leq 3.6$ and epicentral distance smaller than 50 km. The average SSR and HVSR curves, related to the receiver point that represents NRN7 in the model, were shown in figure 7. It is worth noting that, in this case, as explained in the previous paragraph, the SSRs results exactly approach the modelling results (due to the very negligible scattering in the SSR results, see equation 10) and allow us to make a direct comparison between the experimental and numerical amplifications. In both panels of figure 7 the red dotted lines represent the experimental results (the highest amplification function, among all rotations, is indicated) obtained considering the same data sets. In this case the simulations point out amplifications for frequencies around 4-5 Hz, in agreement to the experimental results, but with amplitudes that are underestimated by numerical simulations. The HVSR curves (right panel of figure 7) show a peak around 4 Hz, in agreement with the experimental results. Also in this case the amplification factors obtained from the simulation underestimate those obtained from the experimental analyses.

Seismic response of profile 2

Figure 8 (top panel) shows the general pattern of amplification and deamplification (in terms of transfer functions H_{11}) detected for all receivers located along P2 (NRN4 station, middle panel of figure 8) excited by vertically propagating SV-Ricker wavelets.

The highest amplification occurs around the crest for frequencies in the range 3-6 Hz. As for P1, the bottom panel of figure 8 depicts the time domain response for horizontal component for the profile P2 excited by a vertically incident SV wave. As expected, the maximum amplitude occurred at the top of the hill. As explained before, considering the same data used for P1, even for P2, SSR (the same consideration for profile 1 are valid) and HVSR curves were calculated by equations 8 and 9 (see figure 9). In both panels of the figure the red dotted lines represent the experimental results obtained considering the same data sets. Even in this case the simulations agree well with the experimental results in terms of resonance frequency but show a non-negligible underestimation in terms of amplification factors (up to 2.5).

3D site response : results

To evaluate whether the previously illustrated lower amplification (with respect to the experimental results) from numerical simulations could be explained by the limits of the 2D modelling, we also explored the performance of 3D simulations. For this purpose the *BEMSA* code (Sohrabi et al., 2009), based on boundary element method (BEM), was used. The geometry of the hill and surroundings was modelled using 1224 eight-nodes quadrilateral boundary elements (3729 nodes) and 448 eight-nodes quadrilateral enclosing elements (1289 nodes). The average element size is about 150 m in the neighbourhood of the ridge. The material properties of the model are the same of the 2D model. The layout of the model is shown in figure 10. The accuracy and stability of the results obtained in the time-domain by BEM depend on the combination of space and time discretizations, which is characterized by the dimensionless parameter β (Frangi, 1999), expressed as

$$\beta = \frac{C \cdot \Delta t}{\Delta l} \quad (13)$$

where C , t and l denote the shear wave velocity, the time step and the effective size of the elements respectively. For dynamic analyses of elastic media, accurate and stable results are obtained in the range of $0.2 < \beta < 0.6$ (Frangi, 1999; Von Estorff and Hagen, 2006). In order to satisfy the above criteria, the effective size of the element (l) was assumed to be 75 m on average in the neighbourhood of the topographic irregularity. The value of C was set like 2D modelling (i.e. 1000 m/s) and T was considered as 0.025s. The half space around the topography was discretized up to eight time of the feature dimension, with a gradual increase of spacing between elements. Three independent numerical analyses were performed using incident Ricker wavelets (A_{\max} , f_p and t_0 set to 0.001 m, 3 Hz, and 0.7 s) polarized in X, Y and Z direction. In this way it was possible to derive different components of transfer functions performing a simple convolution analysis as indicated in equation 5. Once the transfer functions were derived, both HVSR and SSR analyses were performed by using equations 8 and 9. As for 2D site response, the computations were performed considering 27 events with $M_L \leq 3.6$ and epicentral distance smaller than 30 km. The results are presented in figure 11 and 12 for the stations NRN7 and NRN4 respectively, that have a similar format as figures 7 and 9. As in the 2D case, the range of frequencies where amplification occurs is rather well captured, but the 3D model turns out not to be sufficient to explain the large observed amplification values.

Significant features of the seismic response of the hill can be captured from figure 13, where the simulated amplification values with respect to an ideal outcropping bedrock are shown. Two frequencies are considered, namely 1 Hz and 4 Hz, close to the fundamental frequency of the hill and to the frequency where experimental amplification factors are larger, respectively. The in-

phase response of the hill at 1 Hz is quite evident, while at a larger frequency such as 4 Hz the peak amplification tends to be clearly delimited along the ridge of the topographic irregularity.

Conclusions

In this paper the results obtained from SSRs and HVSRs computed on experimental data recorded at Narni ridge (central Italy) were compared to those provided by 2D and 3D numerical simulations. The experimental data were recorded in the period March - September 2009 and allowed us to collect a data set including about 700 events with $1.5 \leq M_L \leq 5.3$ and epicentral distance up to 100 km. The analyses computed both using the single station technique (HVSR) and the reference site technique (SSR) highlighted, for the stations installed along the crest (figure 1), the presence of topographic site effects mainly in the frequency range 3.5-5 Hz. The amplification peaks, clearly polarized in the directions perpendicular to the main elongation of the ridge (figure 3 and 4), were detected considering weak motions data (M_L up to 3.6) recorded in near field (up to 30 km). The amplification functions obtained by SSRs calculated for the stations located at the top of the hill reach, in average, values between 4 and 5, with the exception of considering a subset of events characterized by source to site azimuth perpendicular to the main elongation of the ridge: in this case the amplification functions reach values up to 8 (bottom right panel of figure 4). As already demonstrated by many authors (e.g. Spudich et al., 1996; Le Brun et al., 1999; Buech et al., 2010; Massa et al., 2010; Pischiutta et al., 2010; Marzorati et al. 2011), the analyses show that the maxima amplifications appear considering directions perpendicular to the main elongation of the ridge.

Finally, as shown in figure 5, also vertical amplifications (up to 3.5) were detected close to the crest (see top panels of figure 5). More details about the experimental results are available in Massa et al. (2010).

Considering as a target the experimental results, the performance of 2D (profile P1 and P2, bottom panel of figure 1) and 3D (figure 10) numerical modelling was verified. In this case the ridge was considered as an homogeneous and isotropic body and was modelled by using the boundary element method, implemented for 2D and 3D simulations in the codes *HYBRID* (Kamalian et al., 2003) and *BEMSA* (Sohrabi et al., 2009) respectively. As highlighted in figures 7 and 9, for 2D analyses, and 11 and 12, for 3D analyses, the results of numerical modelling well agree with those obtained from the experimental data in terms of frequency range where peak amplification occurs, but in general the amplifications are underestimated by a factor ranging from 2 to 2.5. For the case of Narni, having the ridge a clear bidimensional behaviour, the 3D approach, very expensive in terms of time of calculations, does not show particular improvement if compared to 2D results.

The missing improvement of numerical results from 2D to 3D homogeneous models of the Narni hill, suggests that the observed amplification in the 3-5 Hz frequency range may not be due to topography effects alone, but more likely to coupling of topography and stratigraphy effects. This

confirms the quantitative disagreement between theoretical and observed amplification at topographic features, first noted by Géli et al. (1988) and then confirmed by subsequent observations (Bouchon and Barker, 1996; Spudich et al., 1996; Le Brun et al., 1999). Bouchon and Barker (1996) estimated that a 3D homogeneous numerical model of the well-known Tarzana hill site could explain only 30-40% of the observed amplification, while Paolucci et al. (1999) reached a similar conclusion for the Matsuzaki hill site. In the latter case, in-situ investigations revealed that the site with maximum amplification was characterized by a 15-20 m thick surface layer of strongly weathered rocks. The introduction of such layer in the numerical calculations was sufficient to explain the observed amplifications.

In the case of Narni hill, consisting of massive limestone with a limited degree of fracturation, the importance of such rock weathering modifying the local seismic wave velocities, should be further investigated.

Acknowledgments

This work was funded by the Italian Civil Protection (DPC) in the framework of the 2007-2009 agreement with the Istituto Nazionale di Geofisica and Vulcanologia (INGV). This study is included in task 4 (Identification of anomalous sites and records) of the DPC-S4 project Banca Dati Accelerometrica Italiana (<http://esse4.mi.ingv.it>). We thank the University of Genova (Dip.Te.Ris, <http://dipteris.unige.it/geofisica>) and the INGV-CNT department (url <http://cnt.rm.ingv.it>) for instrumental support in the field experiments, Ezio D'Alema, Stefano Gori, Emanuela Falcucci and Prof. Claudio Eva for useful suggestions and all people of the municipality of Narni for the cooperation during the field experiment.

References

- Amanti, M., R. Bontempo, P. Cara, G. Conte, D. Di Bucci, P. Lembo, N. A. Pantaleone, and R. Ventura (2002). Editors EDS, Carta Geologica d'Italia Interattiva 1:100,000 (Interactive geological map of Italy, 1:100,000), SGN, SSN, ANAS, 3cd-rom.
- Ameri, G., Massa, M., Bindi, D., D'Alema, E., Gorini, A., Luzi, L., Marzorati, M., Pacor, F., Paolucci, R., Puglia, R. and Smerzini, C. (2009). The 6 April 2009, M_w 6.3, L'Aquila (Central Italy) earthquake: strong-motion observations, *Seism. Res. Lett.*, 80, n6, 951-966.
- Bard P. Y. (1982). Diffracted waves and displacement fields over two-dimensional elevated topographies, *Geophys. J. Int.*, 71 731-760.
- Bard P.-Y. and B. E. Tucker (1985). Underground and ridge site effects: a comparison of observation and theory, *Bull. Seism. Soc. Am.*, 75, 905-922.
- Boore D. M. (1972). A note on the effect of simple topography on seismic SH waves. *Bull. Seism. Soc. Am.*, 62, 275-284.
- Borcherdt R.D. (1970). Effects of local geology on ground motion near San Francisco Bay. *Bull. Seism. Soc. Am.*, 60, 29-61.
- Bouchon M. (1973). Effect of topography on surface motion. *Bulletin of the Seismological Society of America*, 63: 615-632.
- Bouchon, M. and Barker, J.S. (1996). Seismic response of a hill: the example of Tarzana, California, *Bull. Seism. Soc. Am.*, 60: 66. 72.
- Brebbia C.A. and Dominguez J. (1989). *Boundary Elements, An Introductory Course*. Computational Mechanics Publications: Boston.
- Buech F., Davies T. R. and Pettina J. R. (2010). The Little Red Hill Seismic Experimental Study: Topographic Effects on Ground Motion at a Bedrock-Dominated Mountain Edifice, *Bull. Seism. Soc. Am.*, vol. 100; no. 5A; p. 2219-2229.
- Chavez-Garcia F., Sanchez L.R. and Hatzfeld D. (1996). Topographic site effects and HVSR. A comparison between observation and theory, *Bull. Seism. Soc. Am.*, 86, 5, 1559-1573.

Faccioli E., Paolucci R., Maggio F., Quarteroni A. (1997). 2D and 3D elastic wave propagation by pseudo-spectral domain decomposition method, *Journal of Seismology* 1, 237-251.

Faccioli E., Vanini M. and Frassinè L. (2002). *Complex Site Effects in Earthquake Ground Motion, including Topography*. 12th European Conference on Earthquake Engineering, Barbican Centre, London, UK.

Frangi A. (1999). Elastodynamics by BEM: a new direct formulation. *International Journal for Numerical Methods in Engineering*; 45:721. 740.

Géli L., Bard P.-Y. and Jullien B. (1988). The effect of topography on earthquake ground motion : a review and new results, *Bull. Seism. Soc. Am.* 78, 42-63.

Kamalian M., Gatmiri B., Sohrabi-Bidar A. (2003). On Time-Domain Two-Dimensional Site Response Analysis of Topographic Structures by BEM. *Journal of Seismology and Earthquake Engineering*, 5:35-45.

Kamalian M., Jafari M. K., Sohrabi-Bidar A., Razmkhah A., Gatmiri B (2006). Time-Domain Two-Dimensional Site Response Analysis of Non-Homogeneous Topographic Structures by A Hybrid FE / BE Method. *Soil Dyn Earthquake Eng*;26:753-765.

Kamalian M., Gatmiri B., Sohrabi Bidar A., Khalaj A. (2007). Amplification Pattern of 2D Semi-Sine Shaped Valleys Subjected To Vertically Propagating Incident Waves. *Communications in Numerical Methods in Engineering*;23: 871-887.

Komatitsch D. and Vilotte J.P. (1998). The Spectral Element Method: An Efficient Tool to Simulate the Seismic Response of 2D and 3D Geological Structures, *Bull. Seism. Soc. Am.*, 88, 368-392.

Israil, A.S.M. and Banerjee, P.K. (1990). *Two-Dimensional Transient Wave Propagation by Time Domain BEM*; *Int. J. Solids and Structures*, 26 (8), 851-864.

LeBrun B., Hatzfeld D., Bard P.Y. and Bouchon M. (1999). Experimental study of the ground motion on a large scale topographic hill at Kitherion (Greece), *Journal of Seism.*, 3, 1-15.

Lermo J. and Chavez-Garcia F.J. (1993). Site effect evaluation using spectral ratio with only one station, *Bull. Seism. Soc. Am.*, 83, 1574-1594.

Marzorati S., Ladina C. , Falcucci E. , Gori S. , Ameri G. , Galadini F. (2011). Site effects on the rock: the case of Castelvechio Subequo (L'Aquila, central Italy), submitted to Bulletin of Earthquake Engineering.

Massa M., Ferretti G., Cevasco A., Isella L. e Eva C. (2004). Analysis of site amplification phenomena: an application in Ripabottoni for the 2002 Molise, Italy, earthquake, Earthquake Spectra, 20, issue S1, 107-118.

Massa M., Lovati S., D'Alema E., Ferretti G. and Bakavoli M. (2010). An experimental approach for estimating seismic amplification effects at the top of a ridge, and the implication for ground-motion predictions: the case of Narni (central Italy), Bull. Seism. Soc. Am., in press.

NTC (Nuove Norme Tecniche per le Costruzioni) (2008). Part 3: Categorie di sottosuolo e condizioni topografiche, Gazzetta Ufficiale n. 29 del 4 febbraio 2008.

Paolucci R. (1999). Numerical evaluation of the effect of cross-coupling of different components of ground motion in site response analyses, Bull Seism Soc Am, 89, 877-887.

Paolucci R., Faccioli E., Maggio F. (1999). 3D Response analysis of an instrumented hill at Matsuzaki, Japan, by a spectral method, Int. Journal of Seismology 3, 191-209.

Paolucci R. (2002). Amplification of earthquake ground motion by steep topographic irregularities. Earth. Eng. and Structural Dynamics, 31, 1831-1853.

Pischiutta M., Cultrera G., Caserta A., Luzi L. and Rovelli A. (2010). Topographic effects on the hill of Nocera Umbra, central Italy, Geophysical Journal International, Vol. 182, 2, 977. 987.

Regione Umbria, direzione politiche territoriali ambiente infrastrutture, servizio geologico (2001). Microzonazione sismica dell'area Narnese Ternana colpita dall'evento sismico del 16 dicembre 2000, Relazione conclusiva, 46 pp.

Rovelli A., A. Caserta, F. Marra and V. Ruggiero (2002). Can seismic waves be trapped inside an inactive fault zone? The case study of Nocera Umbra, central Italy, Bull. Seism. Soc. Am., 92, 2217-2232.

Sanchez-Seisma F. J. (1990). Elementary solutions for response of a wedge-shaped medium to incident SH and SV waves, Bull. Seism. Soc. Am., 80, 737-742.

Sanchez-Sesma F. J. and Campillo M. (1991). Diffraction of P, SV, and Rayleigh waves by topographical features: a boundary integral formulation, *Bull. Seism. Soc. Am.*, 81, 2234-2253.

Sanchez-Sesma F. J., Herrera I. and Aviles J. (1982). A boundary method for elastic wave diffraction: application to scattering SH waves by surface irregularities. *Bulletin of the Seismological Society of America*, 72: 473-490.

Sills, L. B. (1978). Scattering of horizontally polarized shear waves by surface irregularities. *Geophys. J. R. Astron. Soc.*, 54: 319-348.

Smith, W. D. (1975). The application of finite element analysis to body wave propagation problems, *Geophys. J.* 42, 747-768.

Sohrabi Bidar A., Kamalian M., Jafari M.K. (2009). Time-domain BEM for three-dimensional site response analysis of topographic structures. *Int. Journal of Numerical Methods in Engineering*;79:1467-1492.

Spudich P., Hellweg M. and Lee W.H. (1996). Directional topographic site response at Tarzana observed in aftershocks of the 1994 Northridge, California, earthquake: implication for mainshock motion, *Bull. Seism. Soc. Am.*, 86, 193-208.

Von Estorff O. and Hagen C. (2006). Iterative coupling of FEM and BEM in 3D transient elastodynamic. *Engineering Analysis with Boundary Elements*: 30:611. 622.

Zahradnik, J. and L. Urban (1984). Effect of a simple mountain range on underground seismic motion, *Geophys. J. R. Astr. Soc.* 79, 167-183.

Captions

Figure 1 - top panel: wide shot of the Western slope of Narni ridge. Bottom panel: Geological map of the investigated site (Geological Map of Italy, sheet 138, Amanti et al., 2002). Circles indicate the temporary network (in red the stations installed at the base, in blue those installed at the top and in green the just one installed at the middle of the Easter slope). P1 and P2 represent the two transversal profiles (see also the bottom-right inset) considered for 2D modelling.

Figure 2 - Left panel: epicentral location of the earthquakes recorded from 25th March to 7th September 2009. The dimension of circles are related to different M_L . The dotted inset indicates the events with epicentral distance lower than 30 km. Right panel: collected dataset in terms of hypocentral distance versus M_L . Different colours indicate different source to site azimuths.

Figure 3 - Directional HVSRs for stations NRN1 (middle of the slope), NRN2 (base), NRN7 (top) and NRN8 (top) computed considering 10s of S-phase related to 27 earthquakes ($1.5 \leq M_L \leq 3.6$) with epicentral distance lower than 30 km. Different colours indicate averaged amplification functions obtained by the ratio between the Fourier spectrum of each single NS rotated component (36 rotations with step of 5° between 0° and 175°) and the Fourier spectrum of the vertical one.

Figure 4 - Left panels: directional SSRs for stations NRN7. In the top panel the results obtained considering portions of S-phase windows for 27 earthquakes with epicentral distance up to 30 km and M_L up to 3.6 are presented. In the bottom panel the analysis performed on the same data set, but considering 10 s of coda are presented. Right: directional SSRs for stations NRN4. In the top panel the directional SSRs (calculated on S-phase) considering the same 27 events, as selected for NRN7, are shown, while in the bottom panel the results obtained considering a sub-set of 14 events with source to site azimuths perpendicular to the main elongation of the ridge are reported.

Figure 5 - Vertical standard spectral ratio performed considering events with epicentral distance lower than 15 km. For stations 10 and 4 records coming from the L'Aquila sequence ($M_L > 4.5$) are not available. NRN2 represents the reference site.

Figure 6 - Top panel: Amplification and deamplification pattern of horizontal component for frequencies ranging from 0.5 to 8 Hz for vertically SV Ricker wavelet. Middle panel: location of the receivers along the profile P1; the black triangle indicates the location of NRN7 station. Bottom panel: synthetic seismograms for horizontal component of motion, obtained for the receivers shown in the middle panel.

Figure 7 - Left: comparison between 2D modelling (solid thick and thin black lines represent median and standard deviation respectively) and experimental results (dotted red line) for profile 1 (receiver corresponding to NRN7 station). The simulation results are presented in terms of SSRs (see text for explanation) calculated by the ratio between spectra obtained at the top of the topography (multiplying the reference site spectra by the theoretical transfer functions H_{ij}) and the spectra calculated considering real seismograms recorded at the reference site (NRN2).

Right: mean HVSRs (thick black lines) and associated standard deviation (thin black lines) calculated following the same approach used for SSRs, considering a receiver corresponding to NRN7 station (profile 1). The dotted red line represent the experimental result.

Both for SSRs and HVSRs the results were obtained applying the synthetic transfer functions to 27 near field earthquake with epicentral distance up to 30 km and M_L up to 3.6.

Figure 8 - The same as in figure 6, but for profile 2. The black triangle in the middle panel indicate NRN4 station.

Figure 9 - The same as in figure 7, but considering the receiver that corresponds to NRN4 station (profile 2).

Figure 10 - 3D-model configuration. The triangles indicate the stations installed on the ridge during the field experiment: in red the stations at the base, in black those on the crest and in blue the station installed in the middle of the East slope.

Figure 11 - The same as in figure 7, but obtained by 3D numerical modelling: the results are presented for the receiver that corresponds to NRN7 station.

Figure 12 - The same as in figure 7, but obtained by 3D numerical modelling: the results are presented for the receiver that corresponds to NRN4 station.

Figure 13 - Amplification values of Narni hill-top at 1 Hz and 4 Hz obtained by 3D numerical modelling.

Table 1 - Characteristic of the seismic stations employed during the field experiment.

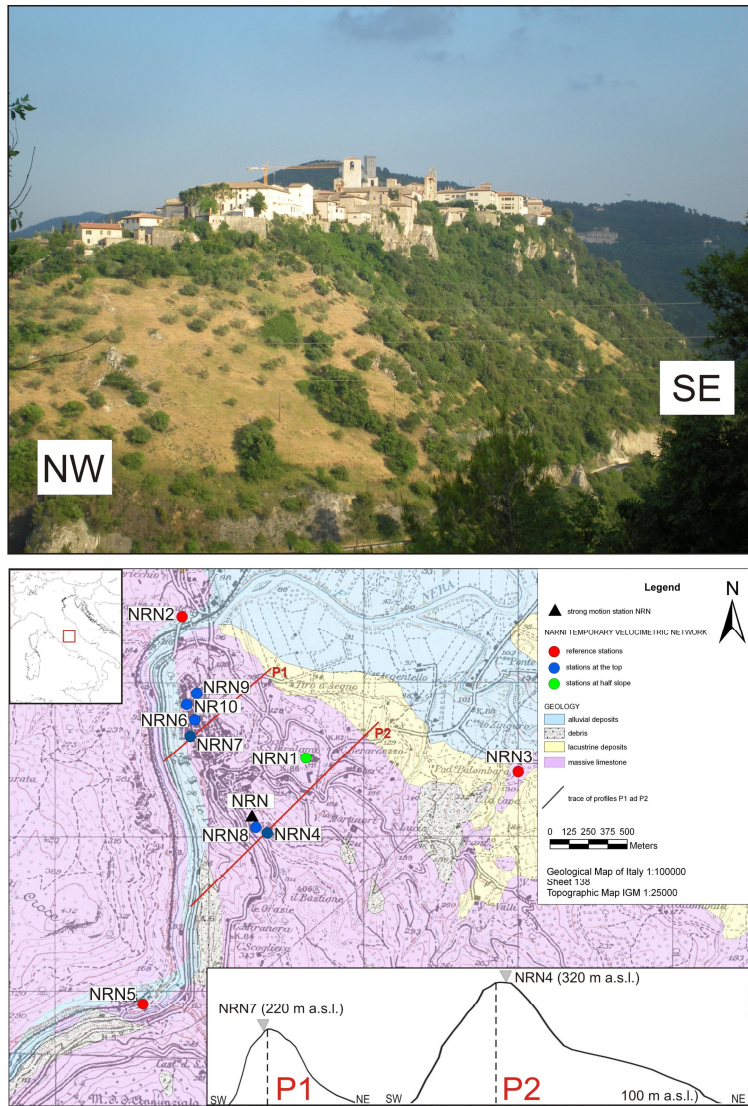


Figure 1

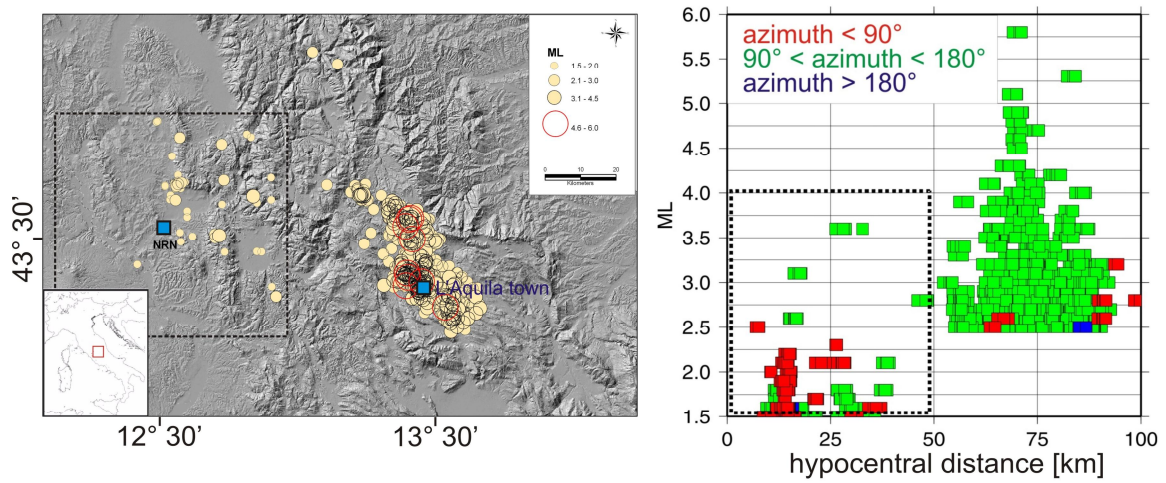


Figure 2

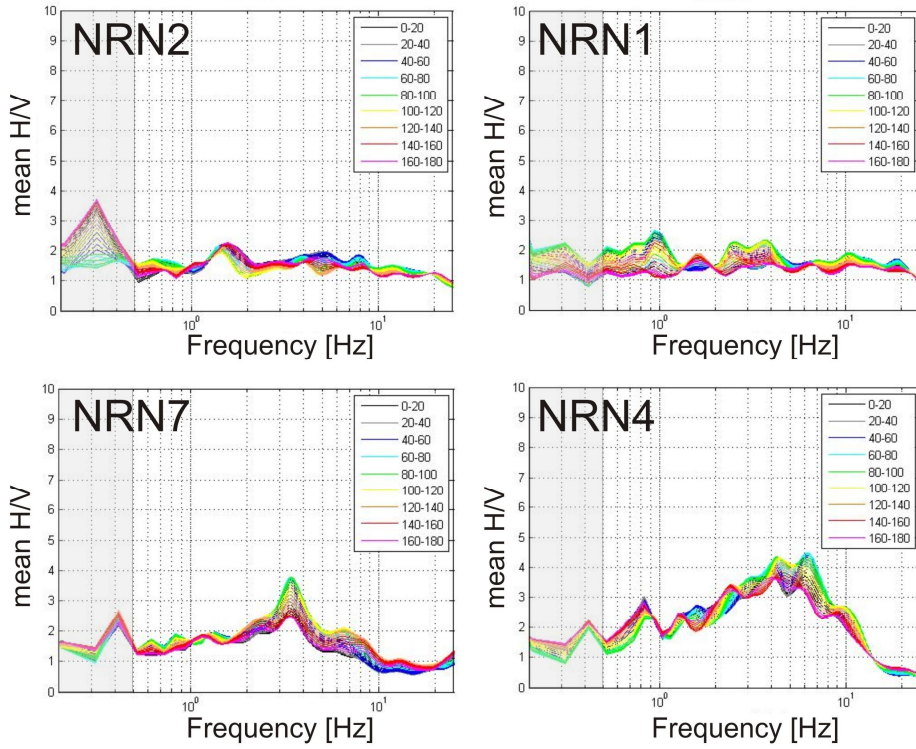


Figure 3

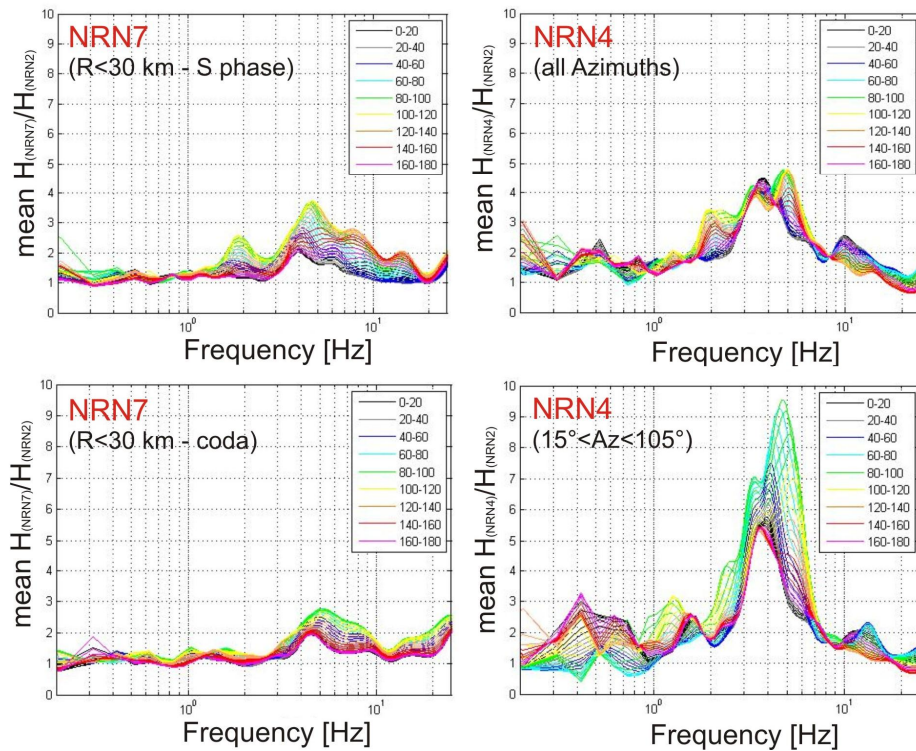


Figure 4

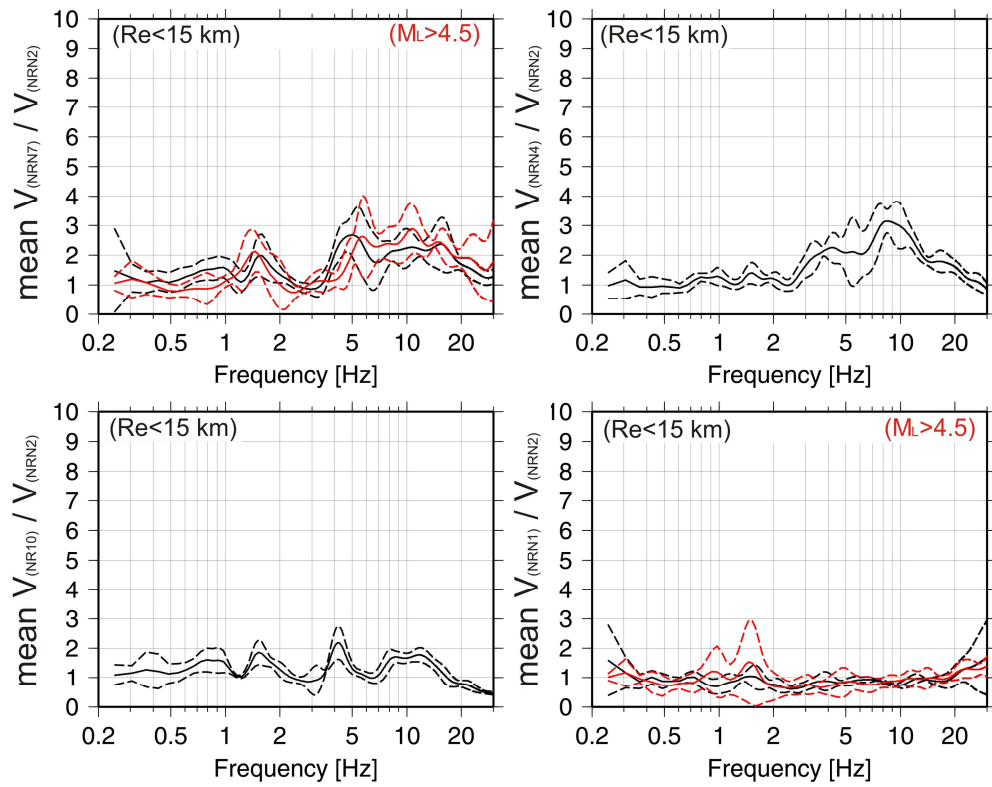


Figure 5

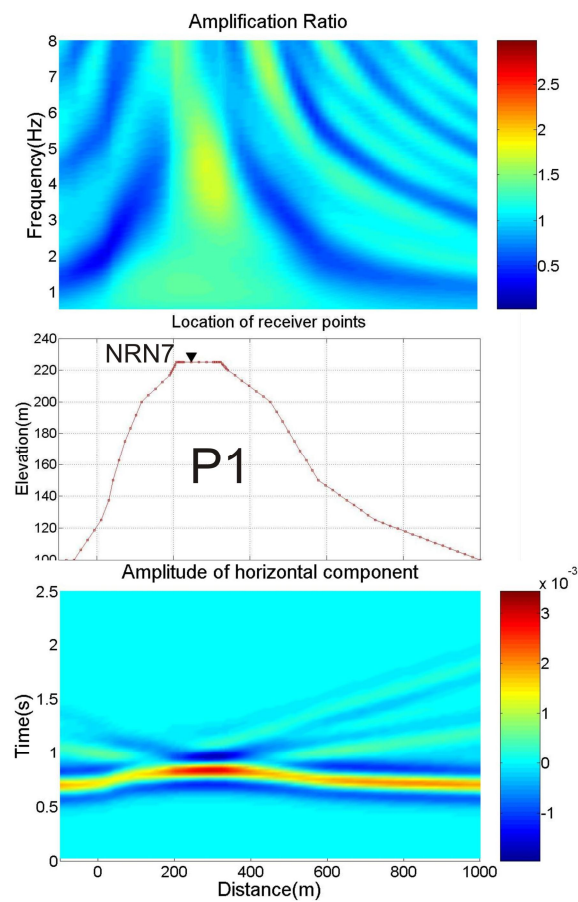


Figure 6

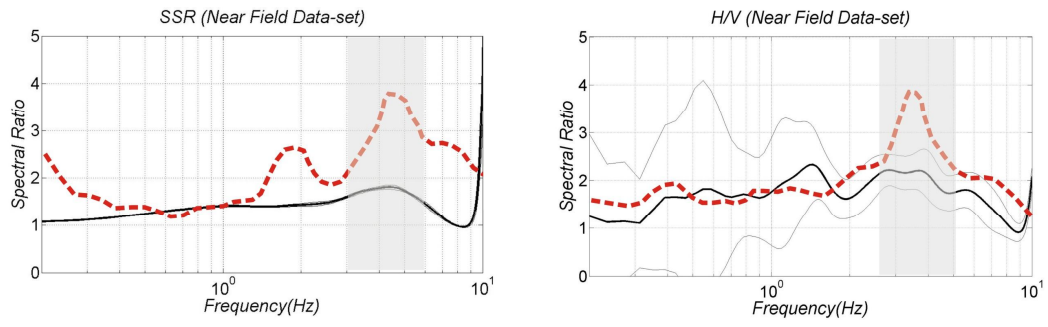


Figure 7

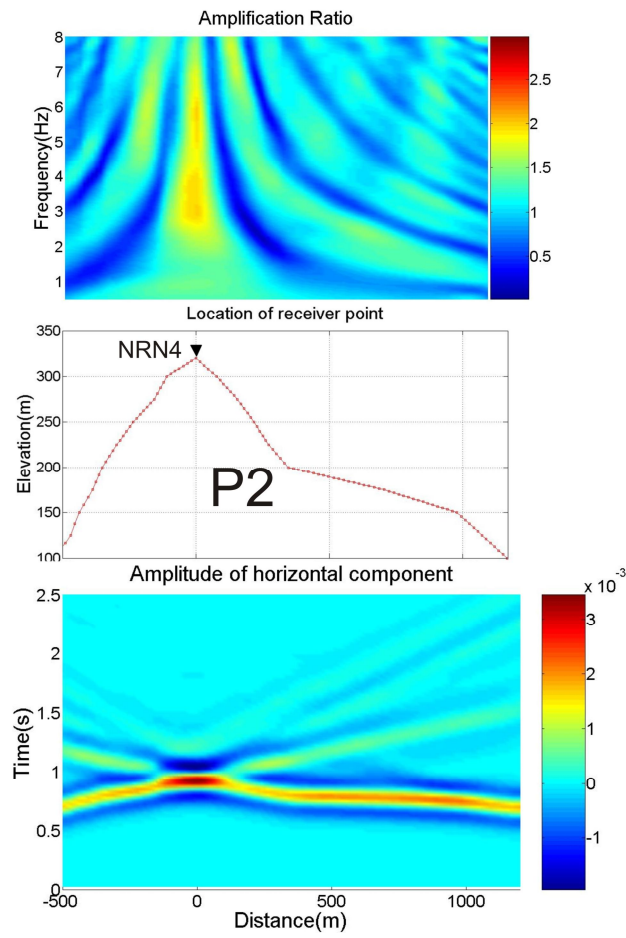


Figure 8

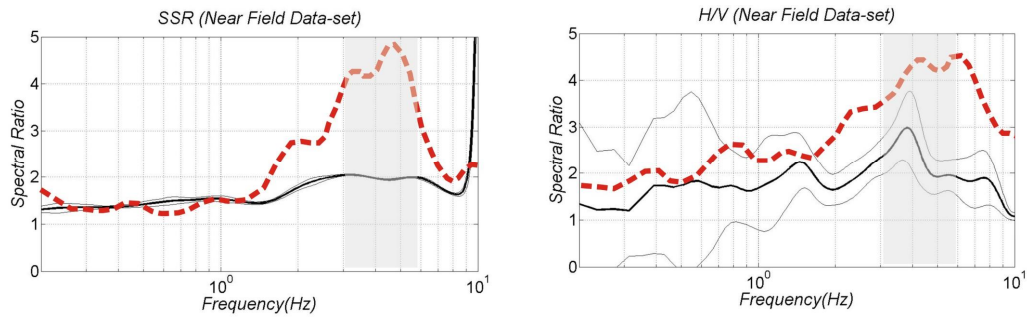


Figure 9

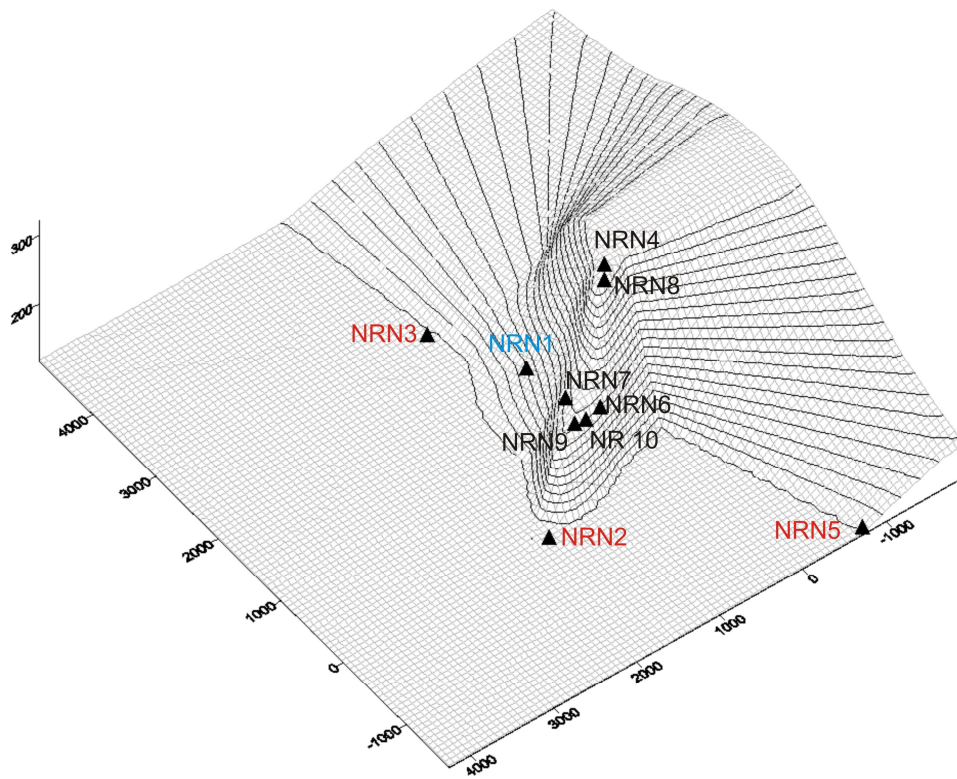


Figure 10

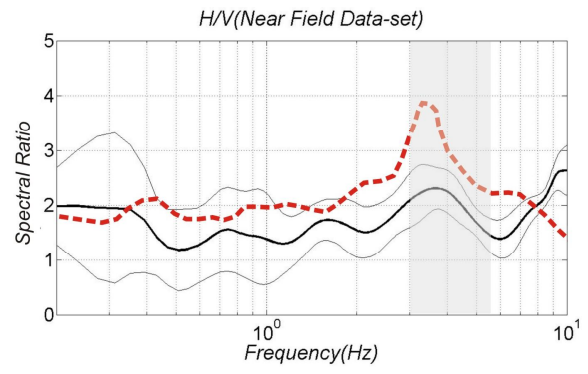
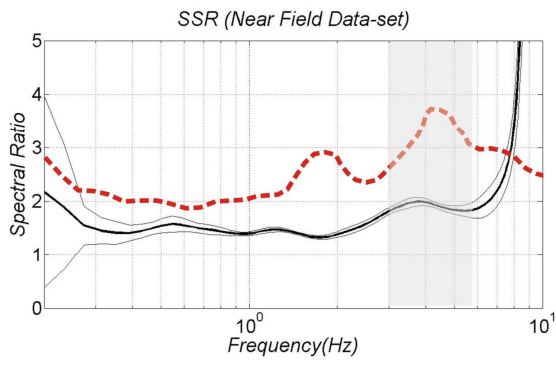


Figure 11

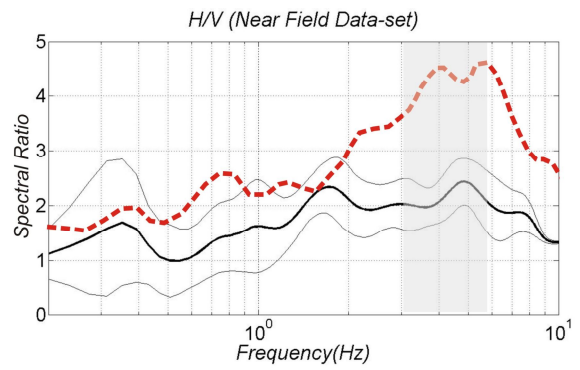
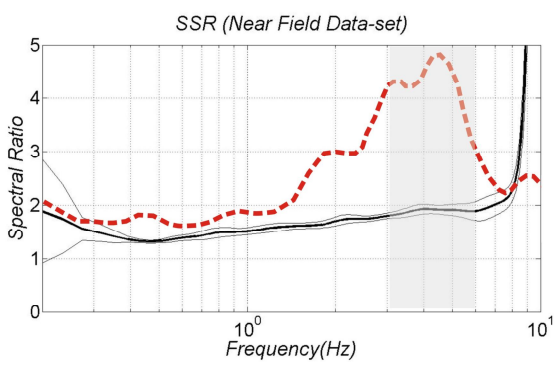


Figure 12

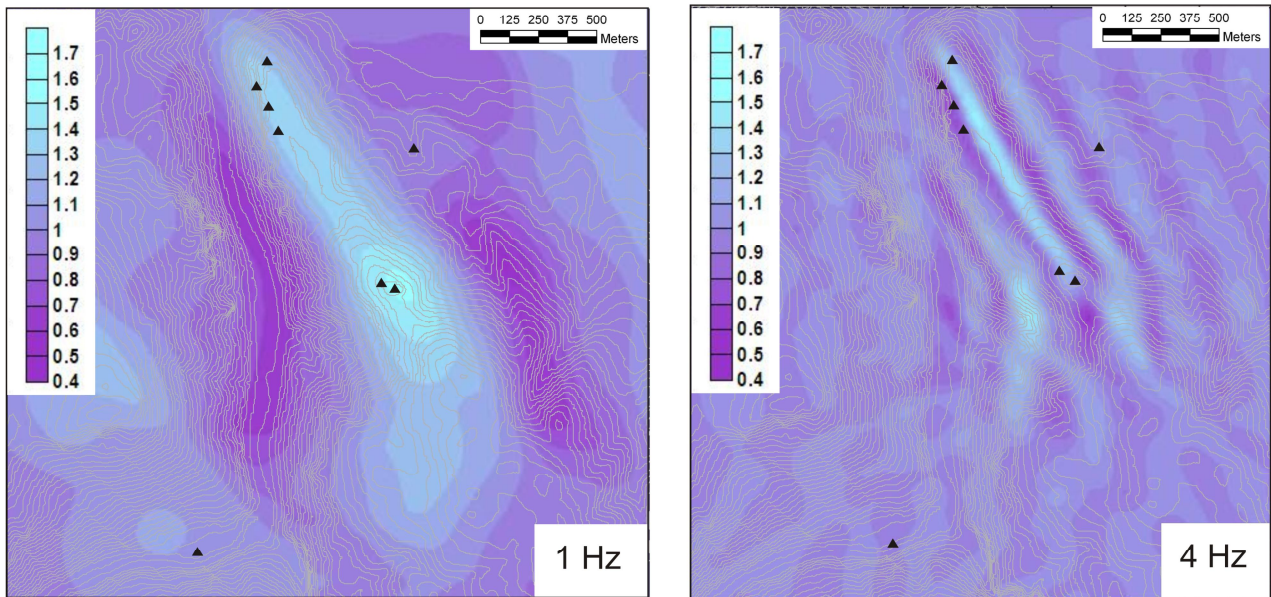


Figure 13

Station	Location	Quota (m a.s.l.)	Sensor	Data logger	Working period
NRN1	middle	180	Lennartz 5s	Reftek-130	25/03/2009-08/06/2009
NRN2	base	105	Lennartz 5s	MarsLite	25/03/2009 - 07/09/2009
NRN3	base	113	Lennartz 5s	Reftek-130	25/03/2009 - 07/09/2009
NRN4	top	320	Lennartz 5s	MarsLite	25/03/2009 - 07/09/2009
NRN5	base	92	Lennartz 5s	Reftek-130	25/03/2009-08/06/2009
NRN6	top	233	Lennartz 5s	Reftek-130	25/03/2009-08/06/2009
NRN7	top	240	Lennartz 5s	Reftek-130	25/03/2009 - 07/09/2009
NRN8	top	316	Lennartz 5s	Reftek-130	15/07/2009 - 07/09/2009
NRN9	top	209	Lennartz 5s	Reftek-130	15/07/2009 - 07/09/2009
NRN10	top	225	Lennartz 5s	Reftek-130	15/07/2009 - 07/09/2009

Table 1